Ductility and Buckling Behaviour of Point-by-Point Wire Arc Additively Manufactured Steel Bars

Conference Paper

Author(s):
Silvestru, Vlad-Alexandru (ID); Ariza, Inés; Taras, Andreas

ORIGINAL ARTICLE

Ductility and Buckling Behaviour of Point-by-Point Wire Arc Additively Manufactured Steel Bars

Vlad-Alexandru SIlvestru[1], Inés Ariza[2], Andreas Taras[1]

Correspondence

Dr. Vlad-Alexandru Silvestru
ETH Zurich
Institute of Structural Engineering
Stefano-Franscini-Platz 5
8093 Zurich, Switzerland
Email: silvestru@ibk.baug.ethz.ch

Abstract

The wire arc additive manufacturing (WAAM) technology in combination with computational design shows a big potential for realising novel force-flow optimised and material-efficient connections. This contribution deals with point-by-point WAAM, a material deposition strategy that allows to place material precisely where structurally needed or aesthetically desired. This could be applied, among others, for realising a novel optimised type of steel nodes between custom-oriented profiles, as they occur in freeform steel-glass grid-shells. In this paper, the structural behaviour of robotically fabricated straight WAAM steel bars under uniaxial tensile and compressive loading is discussed. The focus is set on the ductility exhibited by such components as well as on the buckling behaviour observed under compressive loading. Experimental tests were conducted, both under tensile and under compressive loading to assess the influence of the irregular geometry on the structural performance. Furthermore, it was studied to what extent a prediction of the ductile structural behaviour, of the compressive load-bearing capacity and of the post-buckling behaviour is possible by finite element simulations. This contribution presents and discusses highlights of the obtained results.

Keywords

Wire arc additive manufacturing, Point-by-point deposition, Ductile structural behaviour, Column buckling, Finite element simulation

1 Introduction

In recent years, the potential of the wire arc additive manufacturing (WAAM) technology in combination with computational design for the architecture, engineering and construction (AEC) industry is, on the one hand, increasingly investigated in research and, on the other hand, starting to be applied in representative construction projects. Perhaps the best-known example for the latter is the MX3D footbridge in Amsterdam [1]. Other developed prototypes, which did not yet make it to real projects, like the connector developed by Takenaka Corporation and MX3D [2], the hollow section profiles investigated at Imperial College London [3], or the connections and structures realised at TU Darmstadt [4], are also proof of the significant developments in this field. In terms of WAAM research, a recent review is provided in [5]. Latest AEC-related WAAM research has focused, besides new applications, on a better understanding of the mechanical properties of WAAM steels and on better controlling the printing process (see for example [6]-[9]). Compared to other additive manufacturing (AM) technologies applied for metals, WAAM exhibits significant advantages in terms of limited setup complexity, deposition rates, realisable part sizes, and costs [10]. Depending on the length of the deposited seam, a differentiation between continuous and point-by-point (or dot-by-dot) deposition can be made (see [11]). While most of the current WAAM investigations focus on continuous deposition, point-by-point WAAM allows for producing self-supporting components to be used as reinforcement elements in concrete [12], stand-alone networks [11], [13], or lattice structures [14]. Furthermore, as described by Ariza et al. in [15], such WAAM components fabricated in place can be used for joining non-touching steel profiles as illustrated in Figure 1a.

With future developments, point-by-point WAAM could play a significant role in producing a novel type of steel nodes for freeform grid-shell steel structures, as the one illustrated in Figure 1b. Such nodes in existing structures [16] *(i)* need complex processing of the profile ends to be joined, *(ii)* require to be adaptable due to variable angles between the profiles and, in most cases, *(iii)* use more material than necessary from a structural point of view. WAAM, and especially point-by-point WAAM, could allow significant optimisations in these regards. Previous investigations focusing on topology optimisation of such nodes showed that the material consumption could be significantly reduced by adopting production technologies that allow a targeted distribution of the material (see [17]-[19]). Point-by-point WAAM members to be used in such connections would be subjected to both tensile and compressive forces, depending on the occurring loading scenarios.

1. ETH Zurich, Institute of Structural Engineering, Zurich, Switzerland.
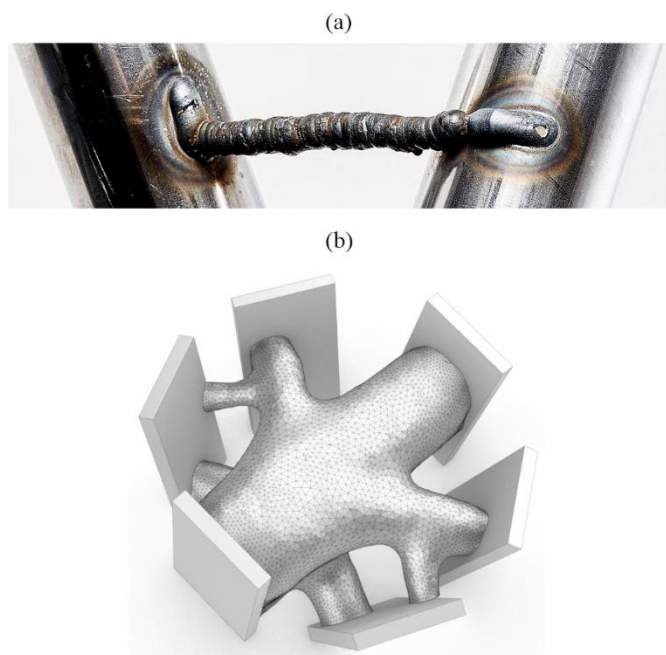2. ETH Zurich, Institute of Technology in Architecture, Zurich, Switzerland.

© 2022 The Authors. Published by Ernst & Sohn GmbH. · ce/papers 5 (2022), No. 4

Figure 1 Example of a robotically produced WAAM-connection with a single bar (© Photography: Catherine Leutenegger) (a) and possible future solution for steel nodes in grid-shell structures with point-by-point WAAM steel components (b). Source: I. Ariza, Gramazio Kohler Research (a) & J. Jäggi, H. Steiner, V.A. Silvestru (b)/ETH Zurich

This paper shows selected results from detailed experimental and numerical investigations performed on straight WAAM bars under tensile and compressive loading. The focus is put on the ductility exhibited by such bars as well as on the importance of the irregular geometry for the structural behaviour of such elements and its prediction by finite element simulations. While tensile tests on point-by-point printed bars were conducted before by several (see [8] and [9] for unalloyed steels and [20] and [21] for stainless steels), compressive buckling tests on such bars could only be found in [21] for a stainless steel.

2 Material properties

The material used for producing the WAAM bars investigated in this paper was Union SG 2-H, a solid wire for gas metal arc welding (GMAW) of unalloyed and low alloy steels [22]. A mixture of 20% carbon dioxide (CO_2) in pure argon (Ar), also known as M21, was applied as shielding gas with a constant flow of 16 L/m. Mechanical properties of WAAM bars printed with this material were determined in [9] based on tensile tests on milled specimens. A Young's modulus of around 195'000 MPa, a yield strength of around 360 MPa, an ultimate strength of around 490 MPa and a failure strain of around 32% were determined.

3 Methods

The methods applied to evaluate robotically produced WAAM steel bars are described in this section and include the fabrication of the bars, their geometrical measurement and evaluation, uniaxial tensile tests, uniaxial compressive tests and finite element simulations for predicting the structural behaviour of such bars.

3.1 Robotic fabrication of WAAM steel bars

The setup used for printing the WAAM bars is shown in Figure 2a. It consisted of an ABB IRB 4600/40 robot, a Fronius TPS 500i Pulse power source and a Fronius 60i Robacta Drive Cold Metal Transfer (CMT) torch with a 22° neck. As substrates, 5 mm steel plates fixed to a stationary welding table of the size of a pallet were used. WAAM steel bars were printed with different angles to the gravity vector (build angle) as well as

with different angles between the bar axis and the axis of the nozzle (nozzle angle). This contribution focuses on results obtained for the WAAM steel bars printed parallel to the gravity vector (build angle of 0°) and with a nozzle angle of 0° (see example in Figure 2b). Detailed results for the bars printed with other angles and tested under tensile loading can be found in [9]. Furthermore, the corrosion behaviour of such bars was investigated in [23]. The results of the WAAM steel bars printed with different angles and tested under compressive loading are being evaluated at the moment of writing this paper and will be presented in a later journal publication.

The printing process consists in depositing a point seam on top of an already solidified seam. For the tensile test specimens, five WAAM bars were produced as a group, while for the compressive test specimens, the group consisted of only three specimens. Printing in groups of bars allows using the idle cooling time between point seams of one bar for depositing seams on the other bars. Details on the printing process and the controlled parameters can be found in [9]. For the tensile and compressive test specimens discussed in this contribution, Table 1 provides the adapted process parameters for each experiment, and Table 2 gives the constant welding, motion and geometric parameters, used in all experiments.
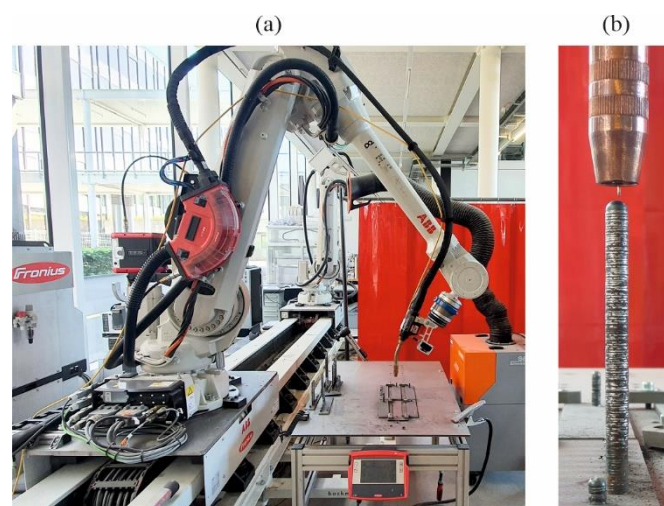
Figure 2 Robotic welding setup (a) and WAAM steel bar during the fabrication process (b). Source: A. Solcà, I. Ariza, V.A. Silvestru/ETH Zurich

3.2 Geometry measurements based on 3D-scanning

After manufacturing the WAAM steel bars, their real geometry was 3D-scanned to evaluate the irregular surface and cross-section development along their length. The photogrammetry-based system GOM Atos Core with its software package was used for the 3D scanning. The instrument incorporating two cameras is set up in a fixed position on a tripod while the specimens are rotated around their longitudinal axis in order to capture a series of pictures. The pictures are then correlated by the GOM software based on markers previously applied in a random pattern. To allow this procedure, both the tensile and compressive test specimens were attached to cylinders at their ends. For the tensile test specimens, steel cylinders were welded to the WAAM steel bars (see Figure 3a and Figure 4a) since these cylinders were also used during the tensile tests for clamping the specimens. For the compressive test specimens, plastic cylinders were bonded adhesively to the ends of the WAAM steel bars just for the geometry measurements. After the measurements, the plastic cylinders were removed. The markers required for correlating the pictures were applied on the cylinders. The WAAM steel bars were sprayed with a negligibly thin matt white paint to avoid reflections. The results of the measurements were very detailed irregular triangular meshes.

Table 1 Adapted process parameters for the tensile test specimens (TS-t) and the compressive test specimens (TS-c)

Series	Number of bars printed as a group	Minimum idle cooling time per droplet [s]	Maximum idle cooling time per droplet [s]	Input process parameters			Output process parameters					
				Current I [A]	Voltage U [V]	Wfs [m/min]	Welding time [s]	Current I [A]	Median I [A]	Voltage U [V]	Median U [V]	Median Wfs [m/min]
TS-t	5	41	66.5	129	13.9	3.5	1.1-1.2	87-130	116	11-15	12.7	2.4
TS-c	3	33	54	120	13.6	3.2	1.1-1.2	97-120	111	12-14.8	13.2	2.6

Table 2 Constant welding, motion and geometric parameters for the tensile test specimens (TS-t) and the compressive test specimens (TS-c)

Wire diameter [mm]	Layer height [mm]	Seam height [mm]	Welding speed [mm/s]	Arc-length correction	Inching value [m/min]	Starting current [%]	Start current time [s]	Slope 1 and 2 [s]	End current [%]	Gas pre flow [s]	Gas post flow [s]
1.2	1.0	1.0	1.0	-4	3.0	135	0.2	1.0	50	0.5	3

The measured geometries were afterwards evaluated with a Grasshopper script in the software Rhinoceros 3D [24]. By cutting the irregular mesh with planes every 0.1 mm along the WAAM bar length (see Figure 3b), the development of the cross-section area was evaluated. Furthermore, on each of the resulting cross-section curves, sixteen points were defined at every 22.5° (see Figure 3c). Based on these points, eight fictive diameters were calculated for each cross-section.
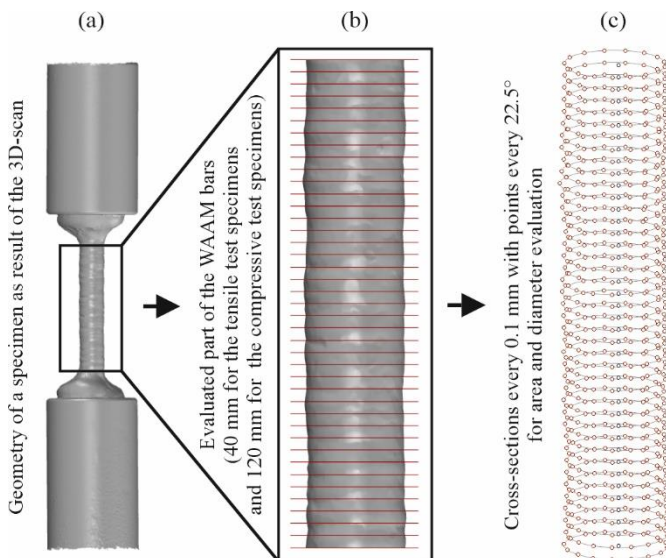

Figure 3 Schematic illustration of the procedure for geometry evaluation based on a uniaxial tensile test specimen: 3D-geometry resulting from scanning (a), cut-out of the WAAM steel bar part to be evaluated with sectional planes (b) and cross-sections and points used for area and diameter evaluation. Source: V.A. Silvestru/ETH Zurich (see also [9])

3.3 Uniaxial tensile tests

The uniaxial tensile tests were planned on the basis of EN ISO 6892-1 [25]. For the design of the test specimen shown in Figure 4a, previously used test specimens in [8] and [21] were used as inspiration. The WAAM bars with a target diameter of 8 mm were welded into 50 mm long cylinders made of S355. The WAAM bars had a total length of 160 mm and a length of 60 mm between the cylinders. The cylinders with a diameter of 30 mm were milled on two sides to allow proper clamping in the test setup (see Figure 4b). This test specimen geometry was used

to avoid a failure of the WAAM bars with irregular surface geometry directly at the clamping points. The tests were conducted displacement-controlled on a Zwick universal testing machine able to apply loads up to 200 kN. A constant displacement rate of 0.01 mm/s was used. Besides the applied load and the traverse displacement, the elongation over an initial gauge length of $L_{0,t}$ = 40 mm was measured with a touching extensometer. Furthermore, a digital image correlation (DIC) system was used to measure strains over a field of view with a height of 80 mm. A VIC-3D 8 system from Correlated Solutions, Inc. with two FLIR 12.3 MP cameras and lenses with a focal length of 60 mm were used for the measurements. More details on the tensile test setup can be found in [9].
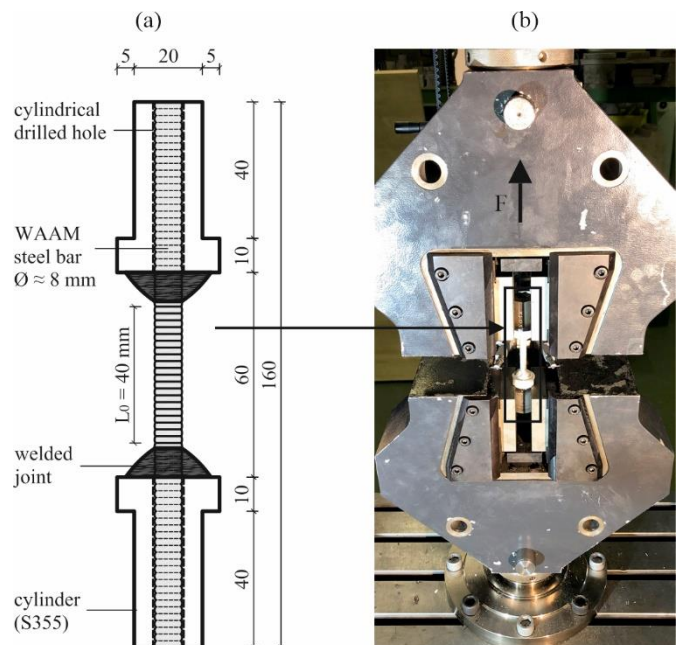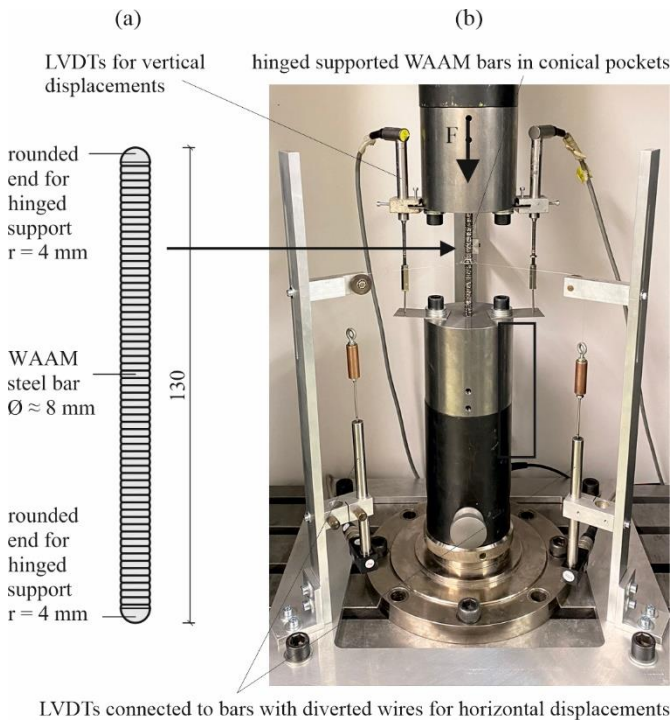

Figure 4 Specimen dimensions for the uniaxial tensile tests (a) and uniaxial tensile test setup (b). Source: V.A. Silvestru/ETH Zurich

3.4 Uniaxial compressive tests

For the uniaxial compressive tests on WAAM bars no suitable standard could be found. Therefore, the specimens and the test setup had to be planned from scratch with a little inspiration from the setup used in [21].

Both hinged-supported and clamped-supported bars were tested; however, only the hinged-supported ones are discussed in this paper. The test specimens consisted of the as-printed WAAM bars with a target diameter of 8 mm and an initial length of 130 mm with the adjustment of rounding their ends to hemispheres with a radius of 4 mm (see Figure 5a). This was done with a turning lathe in order to realise an as-close-as-possible hinged support without using complex machined parts. The counterpart of the rounded ends were conical pockets with a depth of around 4.5 mm and a tip angle of 118°. The test setup with a WAAM-bar with rounded ends fixed into such conical pockets at both ends is illustrated in Figure 5b. To improve the hinged-supported behaviour of the specimens during testing, a grease for reducing friction was applied on the specimen ends.

The tests were conducted displacement-controlled on the same Zwick universal testing machine allowing for maximum loads of 200 kN. A constant displacement rate of 0.005 mm/s was used until a vertical displacement of 1.2 mm was reached (this corresponds to 1% of the approximate distance between the supports of 120 mm). This low initial displacement rate ensures that the peak load is identified correctly. After 1.2 mm vertical displacement, the displacement rate was increased to 0.05 mm/s until a vertical displacement of 12 mm was reached. Single tests were run even longer, but no rupture of the WAAM bars could be reached. In addition to the applied load and the traverse displacement, two linear variable differential transformers (LVDTs) were used to measure the relative vertical displacement between the two cylinders with the conical pockets. Furthermore, three additional LVDTs situated at angles of 120° to each other and connected to the WAAM bars by wires were used to measure the horizontal displacements in the centre of the WAAM bars. These horizontal measurements are, however, not further discussed in this contribution.


Figure 5 Specimen dimensions for the uniaxial compressive tests (a) and uniaxial compressive test setup (b). Source: V.A. Silvestru/ETH Zurich

3.5   Finite element simulations

Finite element simulations were performed for both the tensile and the compressive tests with the computer-aided engineering (CAE) software Abaqus [26]. For the tensile tests only a part equal to the initial gauge length of $L_{0,t}$ = 40 mm was considered, while for the compressive tests

the length between the cylinders with conical pockets of around $L_{0,c}$ = 120 mm was used. These were also the lengths for which 3D-scanning measurements of the real geometry were obtained. Simulations were conducted with the real scanned geometry as well as with constant diameters equal to the target diameter and to the average measured diameter. For the simulations of the compressive tests, also different initial geometric deformations w_0 were considered based on the first eigenmode. For this, first, linear buckling analyses (LBAs) were performed to determine the eigenmodes and, afterwards, geometrically and materially nonlinear analyses with initial geometric imperfections (GMNIAs) were conducted. In the case of the simulations with the real geometry, the very detailed irregular triangular mesh obtained from the 3D-scans was processed with a Grasshopper script in the software Rhinoceros 3D [24] to obtain an equivalent, sufficiently detailed, more regular quad mesh (see Figure 6a). Furthermore, for the compressive test specimens, these quad meshes were aligned with the vertical axis by minimising the average distances of the cross-section centres of gravity to it. Surfaces derived from the quad meshes were then exported to Abaqus, where finite element meshes could be generated for them. 8-node linear brick elements with reduced integration (C3D8R) and a mesh size of 0.5 mm were used for the tensile test simulations, while 20-node quadratic brick elements with reduced integration (C3D20R) and a mesh size of 1 mm were used for the compressive test simulations. The different element types and mesh sizes were the results of convergence studies.
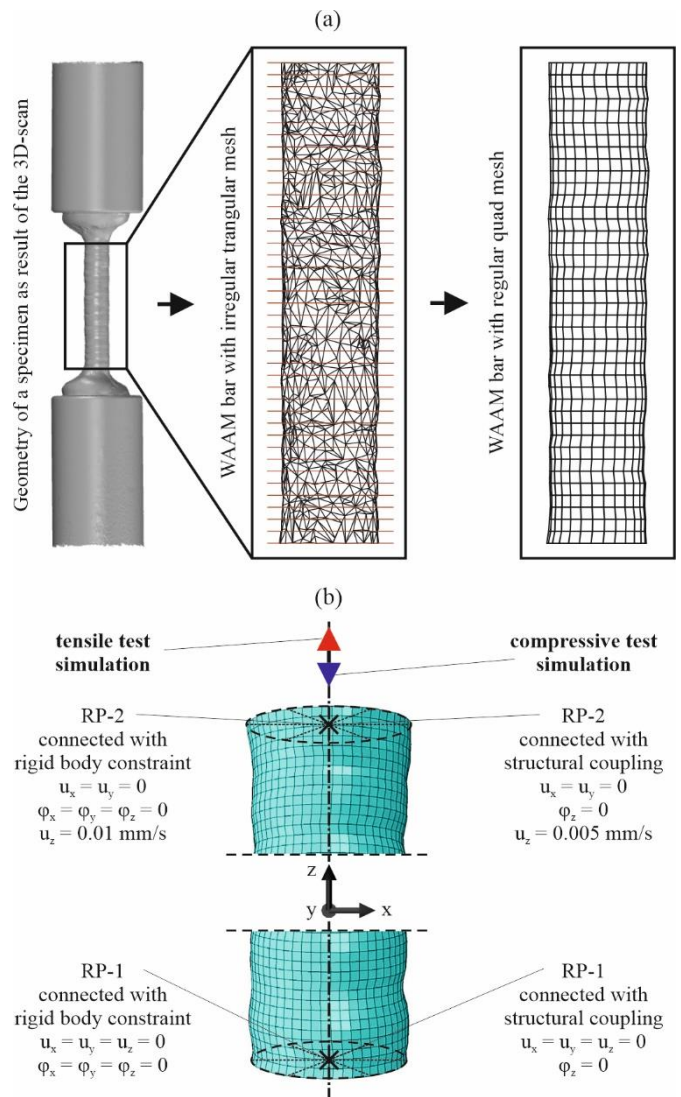
Figure 6 Method for using the real scanned geometry for finite element simulations (a) and characteristics of the simulation models used for the tensile test specimens and for the compressive test specimens (b). Source: V.A. Silvestru/ETH Zurich (see also [9])

Table 3 Yield stress at selected plastic strains as input true values for plastic material properties of the WAAM steel bars

Yield stress	[MPa]	360.0	374.1	442.2	520.6	569.2	606.4	706.3	772.2	864.0	944.6
Plastic strain	[-]	0.000	0.028	0.050	0.100	0.150	0.200	0.400	0.600	1.000	1.500

The boundary conditions and the loading were applied on reference points connected to the end surfaces of the WAAM bars, as illustrated in Figure 6b. For the tensile test simulations, rigid body constraints were used, while for the compressive test simulations, structural coupling constraints were used due to better convergence. The restrained degrees of freedom for the different simulations are shown in Figure 6b.

Elastic and plastic material properties were defined for the WAAM bars. A Young's modulus of $E = 195'000$ MPa and a Poisson's ratio of $v = 0.30$ were used as elastic properties, while for the plastic properties, a series of data pairs of yield stress and plastic strain as true values were defined as shown in Table 3. These values were chosen based on [9].

4 Results and discussion

The results of the different investigations and the interdependencies between them are presented and discussed in this section.

4.1 Evaluation of WAAM steel bars geometry

The point-by-point WAAM steel bars exhibit an irregular surface geometry with varying cross-section shapes and areas along their length. These variations are expected to significantly influence the structural behaviour of such bars both under tensile and under compressive loading. A total of six specimens produced under the conditions described in section 3.1, three of them for the tensile tests and three for the compressive tests, are analysed regarding their geometry in this paper. Two main parameters are used to evaluate the WAAM steel bars geometry: *(i)* the cross-section area and *(ii)* the fictive diameter of the bars. The minimum values, the maximum values, the mean values and the coefficients of variation for these parameters are provided in Table 4 and Table 5, respectively. In general, it can be observed that the values are in relatively similar ranges, both for the tensile and the compressive test specimens. However, it can be noted that especially the minimum values, but also the average values, are a little lower for the tensile test specimens. This could be related to the slightly longer cooling times used for the tensile test specimens, which were printed in a series of five bars, compared to a series of only three bars for the compressive test specimens.

Table 4 Mean value, coefficient of variation (CV), minimum and maximum value from the cross-section area measurements of the two series of WAAM steel bars

Series	Length [mm]	Cross-section area			
		Mean [mm²]	CV [%]	Min. [mm²]	Max. [mm²]
TS-t	40	53.58	4.42	47.02	59.00
TS-c	120	55.87	3.78	49.00	61.17

Table 5 Mean value, coefficient of variation (CV), minimum and maximum value from the diameter measurements of the two series of WAAM steel bars

Series	Length [mm]	Diameter (eight angles per cross-section)			
		Mean [mm]	CV [%]	Min. [mm]	Max. [mm]
TS-t	40	8.25	2.23	7.63	8.87
TS-c	120	8.31	3.08	8.01	8.86

In addition to the tabular values, the variation of the cross-section area along the length of the WAAM bars is plotted in the diagrams from Figure 7. A length of 40 mm equal to the initial gauge length is used for the tensile test specimens (Figure 7a), and a length of 120 mm equal to the approximate distance between the cylinders with the conical pockets is used for the compressive test specimens (Figure 7b). These lengths correspond to the lengths of the bars that could be properly evaluated from the 3D scans. On the one hand, these plots support the provided tabular values. On the other hand, it can be observed that the local variation of the cross-section area is a little more pronounced for the tensile test specimens, while for the compressive test specimens, the average cross-section area is slightly decreasing with increasing bar length (see red dashed trend-line in Figure 7b).
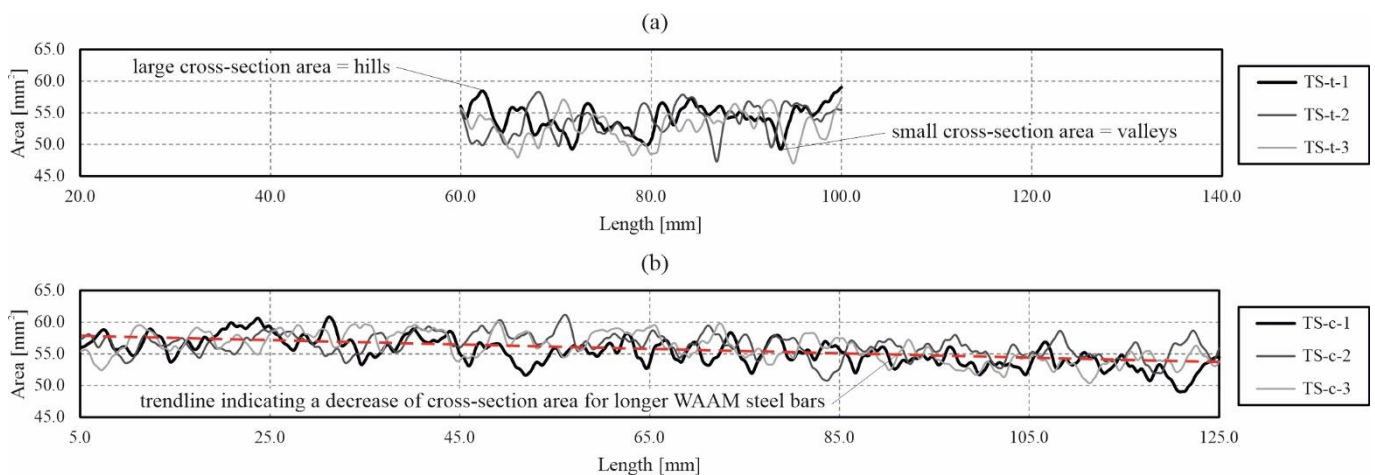
Figure 7 Variation of the cross-section area along a length of 40 mm for the tensile test specimens (a) and along a length of 120 mm for the compressive test specimens (b). Source: V.A. Silvestru/ETH Zurich

4.2 Uniaxial tensile test results

Figure 8 shows the force vs displacement curves for the three tensile test specimens discussed in this contribution. The displacements were calculated based on a virtual extensometer applied to the DIC measurements over a gauge length of 40 mm. A very good agreement between the three curves can be observed for the elastic behaviour and the level of the yield plateau. In the case of the strain hardening, the test specimen TS-t-3 reached slightly lower forces than the other two. This specimen also exhibited the lowest local cross-section area (47.02 mm²) as well as the lowest average value of the cross-section area (52.70 mm²). Moreover, it can be observed that necking occurs for the three specimens at different displacements, also resulting in different maximum reached displacements at failure.
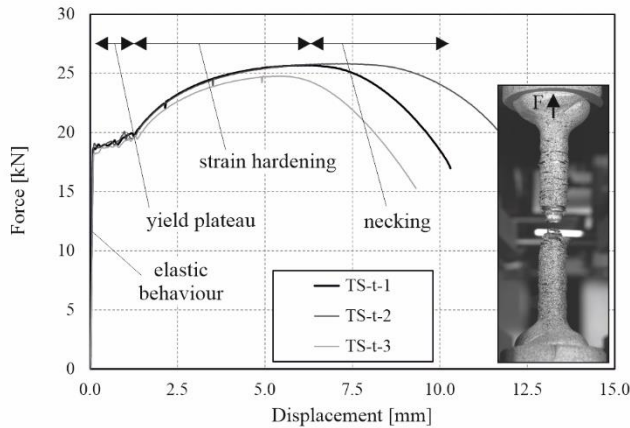
Figure 8 Force vs displacement curves from the uniaxial tensile tests. Source: V.A. Silvestru/ETH Zurich

Besides the curves in Figure 8, selected properties are provided as minimum values, mean values and coefficients of variation in Table 6. The strength values were determined based on the mean cross-section area calculated from the 3D scans and are only a little lower than the values determined for milled specimens in [9].

Table 6 Minimum values, mean values and coefficients of variation for selected properties determined based on the tensile tests

Property	Min. value	Mean value	CV [%]
Maximum load [kN]	24.77	25.43	2.25
Upper yield strength [MPa]*	344.75	349.28	1.85
Tensile strength [MPa]*	470.11	474.62	1.06
Strain at tensile strength [%]	13.80	15.63	12.20
Elongation at failure [%]	23.30	26.88	15.86

* The strength values were determined based on the mean cross-section areas measured for the WAAM steel bars.

In the case of steels for structural applications, existing standards request a minimum ductility. According to the Eurocode [27], three different limits have to be met:

− The ratio between the ultimate strength f_u and the yield strength f_y needs to be higher than 1.10. For the given WAAM bars with the mean values in Table 6, this limit is met by Equation (1):

$$f_u/f_y = 474.62/349.28 = 1.36 > 1.10 \tag{1}$$

− The elongation at failure needs to be at least 15%. This limit is met based on the values in Table 7, even by the lowest maximum elongation of 23.30% determined for specimen TS-t-3.

− The strain corresponding to the ultimate strength has to be higher than 15 times the yield strain. This limit is met based on the values from Table 7 by Equation (2):

$$\varepsilon_u = 13.80\% = 15 \cdot f_y/E = 15 \cdot 349.28/195'000 = 2.69\% \tag{2}$$

This proves that the point-by-point WAAM bars successfully meet the ductility requirements necessary for structural applications.

4.3 Uniaxial compressive test results

Figure 9 shows the force vs displacement curves for the three compressive test specimens discussed in this contribution. A relatively good agreement can be observed both for the pre-buckling and the post-buckling behaviour. The variation of the reached maximum force can be considered small, when taking into account the irregular geometries of the bars.
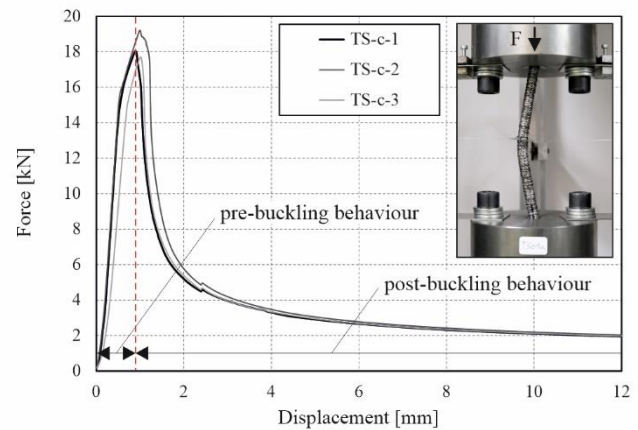
Figure 9 Force vs displacement curves from the uniaxial compressive tests. Source: V.A. Silvestru/ETH Zurich

In addition to the curves in Figure 9, the mean values of selected properties from the tests are given in Table 7. The stresses at the maximum load were determined based on the mean cross-section areas calculated from the 3D scans. It can be observed that these stresses are lower than the yield strength determined in the tensile tests. This indicates that no yielding (or only very local yielding in the smallest cross-sections) is occurring before buckling.

Table 7 Mean values and coefficients of variation for selected properties determined based on the compressive tests

Property	Mean value	CV [%]
Maximum load [kN]	18.32	4.32
Corresponding displacement [mm]	0.97	6.61
Stress at maximum load [MPa]*	327.75	3.80

* The stress values were determined based on the mean cross-section areas measured for the WAAM steel bars.

Figure 10 shows the specimen TS-c-1 at the beginning (Figure 10a) and the end (Figure 10b) of the test, the end corresponding approximately to

a vertical displacement of 12 mm. The shape of the WAAM bar confirms that the used test specimen geometry and setup work well for obtaining hinged supports. Furthermore, the large horizontal deformations without leading to cracks emphasise the highly ductile behaviour of the material.
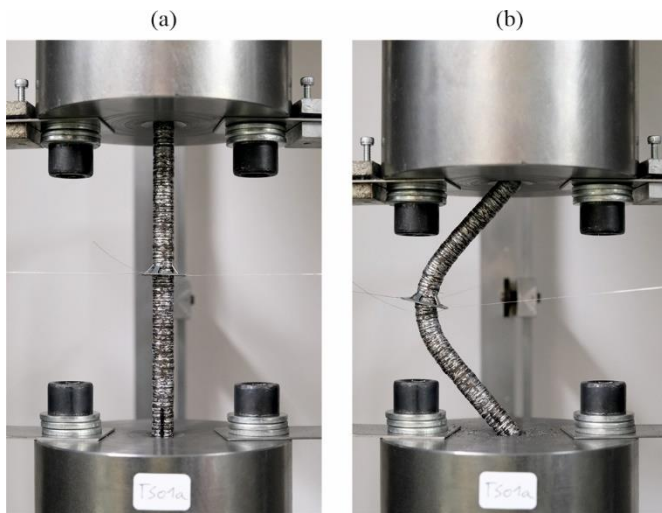
Figure 10 Test specimen at the beginning (a) and the end (b) of the compressive tests. Source: V.A. Silvestru/ETH Zurich

## 4.4   Comparison of experimental and simulation results

Figure 11a shows a comparison between the experimentally obtained force vs displacement curve for the tensile test on specimen TS-t-1 and different curves obtained from finite element simulations of the test.
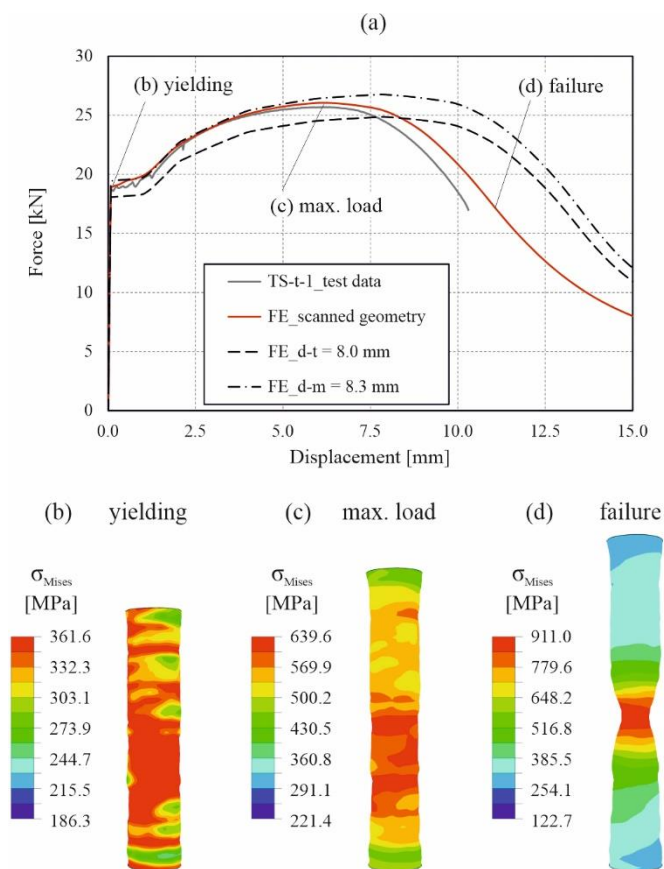
Figure 11 Comparison between the force vs displacement curves from the simulations and the tensile test on specimen TS-t-01 (a) and approximate Mises true stress distribution at yielding (b), at the maximum load (c) and at failure (d). Source: V.A. Silvestru/ETH Zurich

A relatively good agreement is obtained for all parts of the experimental curve when running the simulation with the scanned geometry (red curve in the diagram). When using an equivalent constant diameter, a suitable agreement is reached with the mean measured diameter for the elastic part, the yielding plateau and most of the strain hardening. However, the maximum reached force and the maximum displacements, especially in the necking part, are overestimated. Figures 11b-d show the Mises true stress distributions in the WAAM bar at different characteristic points of the force vs displacement curves from the simulation of the tensile test on TS-t-1 with the scanned geometry. They show that at yielding, higher stresses extend over most of the bar, while towards reaching the maximum load and especially during necking, the peak stresses concentrate more locally.

Figure 12a shows a comparison between the experimentally obtained force vs displacement curve for the compressive test on specimen TS-c-1 and different curves obtained from finite element simulations of the test. It can be noticed that all the simulations behave stiffer than the experiment, which was also observed in previous studies on the behaviour of steel elements under compression. In terms of maximum reached force, a relatively good prediction can be made using the scanned geometry and no additional initial imperfections (red curve in the diagram).
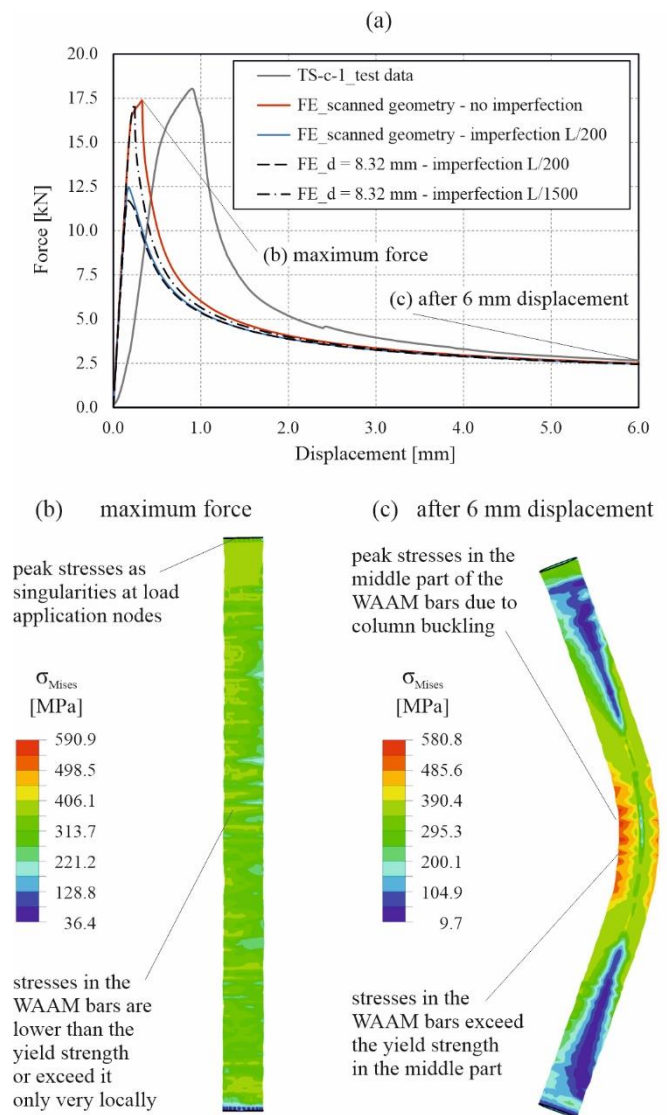
Figure 12 Comparison between the force vs displacement curves from the simulations and the compressive test on specimen TS-c-01 (a) and approximate Mises true stress distribution at the maximum load (b) and after a vertical displacement of 6 mm (c). Source: V.A. Silvestru/ETH Zurich

Similarly, good results are obtained with an effective constant diameter equal to the mean measured diameter and a very small initial deformation $w_0 = L_{0,c}/1500$. However, when using an initial deformation $w_0 = L_{0,c}/200$, as suggested in standards (e.g. [27]) for rods with round cross-sections, the maximum force is underestimated significantly, both in the case of using a constant mean diameter or in the case of using the scanned geometry. This result indicates that the irregular geometry of the WAAM bars has a kind of stabilising effect on the buckling susceptibility. This is very probably due to the fact that the varying cross-sections along the length of the columns are shifted related to the central longitudinal axis in random directions instead of in one direction as it would be for an assumed initial deformation.

Figures 12b-c show the Mises true stress distributions in the WAAM bars when reaching the maximum force and after a vertical displacement of 6 mm. It can be noticed that until reaching the maximum force, the stresses in the bars are below the yield strength (except maybe at the load introduction points and very locally). In the post-buckling phase, the yield strength is exceeded in the middle of the bars where significant bending is occurring.

5   Conclusions and outlook

The investigations discussed in this contribution on the tensile and compressive behaviour of point-by-point WAAM steel bars lead to the following conclusions, which have significant relevance for further developments of this technology for structural applications:

−   The irregular geometry of point-by-point WAAM bars is dependent on the process parameters as well as on the length of the bars.
−   Point-by-point WAAM bars robotically fabricated from the applied solid wire exhibit a suitable ductility for structural applications, in agreement with the Eurocode requirements.
−   Point-by-point WAAM bars behave well under compressive loading, reaching similar buckling resistances as rods with an equivalent constant diameter and very low initial global deformations (around $L/1500$). The irregular shape and cross-section development along the length of the bars seem to have a stabilizing effect on the buckling susceptibility.
−   Finite element simulations with the scanned irregular geometry and elastic-plastic material properties allow for good predictions of the structural resistances under tensile and compressive loading. When using an equivalent constant diameter, partially suitable predictions are possible with the mean diameter.

Some of the topics on which future investigations related to point-by-point WAAM bars should focus are *(i)* the optimisation and control of the process for target dimensions, *(ii)* the fatigue behaviour of such bars with irregular geometry and *(iii)* the digital design, robotic fabrication and structural evaluation of components (e.g. structural nodes) consisting of several such bars.

References

[1]   Gardner, L., Kyvelou, P., Herbert, G., Buchanan, C. (2020) *Testing and initial verification of the world's first metal 3D printed bridge*. J. Constr. Steel Res. 172, 106233.

[2]   MX3D (2019) Connector for Takenaka. Accessed 1 April 2021: https://mx3d.com/industries/construction/connector-for-takenaka/.

[3]   Kyvelou, P., Huang, C., Gardner, L., Buchanan, C. (2021) *Structural Testing and Design of Wire Arc Additive Manufactured Square Hollow Sections*. J. Struct. Eng. 147(12), 04021218.

[4]   Lange J., Feucht, T., Erven, M. (2020) *3D printing with steel – Additive manufacturing for connections and structures*. Steel Constr. 13(3), 144-153.

[5]   Treutler, K., Wesling, V. (2021) *The Current State of Research of Wire Arc Additive Manufacturing (WAAM): A Review*. Appl. Sci. 11, 8619.

[6]   Huang, C., Kyvelou, P., Zhang, R., Ben Britton, T., Gardner, L. (2022) *Mechanical testing and microstructural analysis of wire arc additively manufactured steels*. Mater. Des. 216, 110544.

[7]   Kyvelou, P., Slack, H., Mountanou, D.D., Wadee, M.A., Britton, T.B., Buchanan, C., Gardner, L. (2020) *Mechanical and microstructural testing of wire and arc additively manufactured sheet material*. Mater. Des. 192, 108675.

[8]   Müller, J., Grabowski, M., Müller, C., Hensel, J., Unglaub, J., Thiele, K., Kloft, H., Dilger, K. (2019) *Design and Parameter Identification of Wire and Arc Additively Manufactured (WAAM) Steel Bars for Use in Construction*, Met. 9(7), 725.

[9]   Silvestru, V.A.; Ariza, I.; Vienne, J.; Michel, L.; Aguilar Sanchez, A.M.; Angst, U.; Rust, R.; Gramazio, F.; Kohler, M.; Taras, A. (2021) *Performance under tensile loading of point-by-point wire and arc additively manufactured steel bars for structural components*. Mater. Des. 295, 109740.

[10] Jin, W., Zhang, C., Jin, S., Tian, Y., Wellmann, D., Liu, W. (2020) *Wire Arc Additive Manufacturing of Stainless Steels: A Review*. Appl. Sci. 10(5), 1563.

[11] Laghi, V., Palermo, M., Gasparini, G., Trombetti, T. (2020) *Computational design and manufacturing of a half-scaled 3D-printed stainless steel diagrid column*. Addit. Manuf. 36, 101505.

[12] Mechtcherine, V., Grafe, J., Nerella, V.N., Spaniol, E., Hertel, M., Füssel, U. (2018) *3D-printed steel reinforcement for digital concrete construction – Manufacture, mechanical properties and bond behaviour*. Constr. Build. Mater. 179, 125-137.

[13] Radel, S., Diourte, A., Soulié, F., Company, O., Bordreuil, C. (2019) *Skeleton arc additive manufacturing with closed loop control*. Addit. Manuf. 26, 106-116.

[14] Abe, T., Sasahara, H. (2019) *Layer geometry control for the fabrication of lattice structures by wire and arc additive manufacturing*. Addit. Manuf. 28, 639-648.

[15] Ariza, I., Mirjan, A., Gandia, A., Casas, G., Cros, S., Gramazio, F.,

Kohler, M. (2018) *In place detailing: Combining 3D printing and robotic assembly*. In: Anzalone, P., Del Signore, M., Wit, A.J. (eds.) ACADIA 2018 Recalibration: On Imprecision and Infidelity, Proceedings of the 38th Annual Conference of the Association for Computer Aided Design in Architecture, 312-321.

[16] Stephan, S., Sanchez-Alvarez J., Knebel K. (2004) Stabwerke auf Freiformflächen. Stahlbau 73, 562-572.

[17] Seifi, H., Javan, A.R., Xu, S., Zhao, Y., Xie, M.Y. (2018) *Design optimization and additive manufacturing of nodes in gridshell structures*. Eng. Struct. 160, 161-170.

[18] Prayudhi, B. (2016) *3D3D: Form Follows Force with 3D printing – Topology Optimization for Free-form Building Envelope design with Additive Manufacturing*. MSc thesis, TU Delft.

[19] Wang, H., Wenfeng, D., Zhao, Y., Wang, Y., Hao, R., Yang, M. (2021) *Joints for treelike column structures based on generative design and additive manufacturing*. J. Constr. Steel Res. 184, 106794.

[20] Laghi, V., Palermo, M., Tonelli, L., Gasparini, G., Girelli, V.A., Ceschini, L., Trombetti, T. (2022) *Mechanical response of dot-by-dot wire-and-arc additively manufactured 304L stainless steel bars under tensile loading*. Constr. Build. Mater. 318, 125925.

[21] Joosten, S. (2015) *Printing a Stainless Steel Bridge – An exploration of structural properties of stainless steel additive manufactures for civil engineering purposes*. MSc thesis, TU Delft.

[22] Union SG 2-H: Solid wire, unalloyed (2014), Product data sheet, Böhler welding by voestalpine.

[23] Michel, L., Sanchez, A.M.A., Silvestru, V.A., Ariza, I., Taras, A., Angst, U. (2022) *Corrosion behaviour of point-by-point wire and arc additively manufactured steel bars*. Mater. Corros., 1-19.

[24] McNeel, R. & others (2021), Rhinoceros 3D, Version 7.0 SR10, Robert McNeel & Associates, Seattle, WA, USA.

[25] EN ISO 6892-1 (2017) *Metallic materials – Tensile testing – Part 1: Method of test at room temperature*.

[26] Abaqus 2021 (2020), Dassault Systemes Simulia Corp., Johnston, RI, USA.

[27] EN 1993-1-1 (2010) *Eurocode 3: Design of steel structures – Part 1-1: General rules and rules for buildings*.